J. Fluid Mech. (1985), vol. 159, pp. 409–431
Printed in Great Britain

Turbulent stirring in an experimental induction furnace

By E. TABERLET AND Y. FAUTRELLE
INPG – GIS Madylam B.P. 68, 38402 Grenoble Cedex, France

(Received 2 February 1985 and in revised form 29 April 1985)

This paper describes an experimental study of the electromagnetic stirring in a mercury induction furnace. The 200 mm-diameter furnace is supplied with a single-phase electric current of frequency 50–4700 Hz. The flow pattern is measured by means of a special two-wire probe, which tracks the thermal wake behind a hot-film probe. The magnitudes of fluctuating velocities are measured by hot-film anemometry. Attention is focused on the influence on the mean and turbulent motion of the electromagnetic-skin depth, which is determined by the supply frequency. The measurements of the mean motion show that, for a fixed magnetic field, stirring is maximum when the value of the skin depth normalized by the pool radius is about 0.2, in agreement with previous theoretical predictions. Two turbulence regimes may be distinguished for different frequency ranges. At low frequency the various properties of the turbulence, such as the mean-square fluctuations, the integral scales and the turbulent dissipation rate, are almost uniform over the whole bath. However, at high frequency the turbulence is non-uniform; there is an increase in the turbulent fluctuations and dissipation rate and a decrease of the integral scale within the electromagnetic-skin depth near the wall.

1. Introduction

In an induction furnace used for melting and stirring a liquid metal in a crucible, a metal ingot is located in a coil supplied with an alternating current source. The electric current induced in the metal by the external magnetic field creates efficient Joule heating as well as an electromagnetic force field. These forces are generated by the interaction between the induced current and the magnetic field and are responsible for the vigorous turbulent stirring of the bath.

Although there are some drawbacks, such as refractory-wall erosion, the stirring phenomenon has many metallurgical applications which have contributed to the development of such a process. The most important consequences of the stirring and the associated turbulence are:

(i) a good homogeneity of the bath,

(ii) the acceleration of mass transfer, for example the deoxidation and the desulphurization.

These effects come from two distinct phenomena occurring in the liquid metal pool: mixing and particle coalescence. Mixing is a function of the large-scale properties of the turbulence of the flow, whilst particle coalescence is related to the smallest structures of the motion. It is clear that the optimization of these metallurgical effects requires an extensive knowledge of both the mean and turbulent properties of the liquid metal being stirred.

From a fundamental point of view, such recirculating flows present two interesting

original features. Firstly, in respect of the frequency f of the magnetic field the electromagnetic body forces may be confined to a thin wall layer such that

$$\delta = \left(\frac{2}{\mu\sigma\omega}\right)^{\frac{1}{2}}, \quad \omega = 2\pi f, \tag{1}$$

where μ and σ respectively denote the magnetic permeability and the electrical conductivity of the metal. The flow is thus driven by a force field which contains two varying spatial scales, namely the radius of the pool a and the skin depth δ. The influence of this last scale on the mean movement and the turbulence is one of the original aspects of this problem. The magnitude of the inductive current I determines the amplitude of the magnetic field B_0 and the Alfvén's speed u_A, defined from B_0 as follows:

$$u_A = \frac{B_0}{(\mu\rho)^{\frac{1}{2}}}, \tag{2}$$

where ρ is the density of the metal.

It is interesting to note that it is possible to control the intensity of the mixing or more specifically the mechanical power of the mixing by simply acting on parameter I (or u_A).

The effects of the two dimensional parameters δ and u_A, which represent respectively the frequency and the magnitude of the induction currents, are better expressed in terms of the dimensionless parameters R_ω and R_e:

$$R_\omega = \mu\sigma\omega a^2 = \frac{2a^2}{\delta^2}, \quad R_e = \frac{u_a a}{\nu}, \tag{3}$$

where ν represents the viscosity of the liquid metal. These two dimensionless numbers can be derived directly from the Maxwell and Navier–Stokes equations, using the scales B_0, a and u_A (Fautrelle 1981).

The flows of liquid created by single-phase alternating magnetic fields have been studied both theoretically and experimentally in many published papers. The experimental works consist mainly of temperature and speed measurements in mercury modelling (Bednarz 1970; Tarapore & Evans 1976; Cremer & Alemany 1981; Moore & Hunt 1983, 1984; Trakas, Tabeling & Chabrerie 1984; Koanda & Fautrelle 1982). The supply frequencies that have been studied varied from 50 to 5000 Hz, which corresponds to a range of R_ω varying between about 1 and 400. The measurements were achieved either with a hot-film anemometer or by a drag probe (Moore & Hunt 1983), or by stroboscopic photography of the free surface (Tarapore & Evans 1976). Best results occur when the parameter δ/a is a unit. These are the more specifically mean and turbulent velocity measurements of Moore & Hunt (1983, 1984), Trakas *et al.* (1984). Mean flows observed consist normally of two vortices in a half-meridian plane, the dimensions of which are not very sensitive to the parameter of intensity I. On the other hand, the amplitude of mean and turbulent speeds is proportional to I but independent of the frequency. In the range of frequencies studied ($f > 50$ Hz), the influence of the pulsating part of the Lorentz forces remains negligible. Therefore the characteristics of the turbulence (i.e. spectra) remain on the whole similar to those of classical shear flows (Trakas *et al.* 1984). Moore & Hunt (1983), however, have made some noteworthy observations concerning long-period fluctuations.

In the case of weak electromagnetic skins, there has not been a great deal of experimental study. Owing to the small number of experiments undertaken (Cremer

& Alemany 1981; Koanda & Fautrelle 1982) questions still remain to be answered. They concern especially the influence of the scale δ on both the mean flow and the turbulence linked to it.

The aim of the experiment described here was to study the influence of the frequency parameter over a larger range than in previous experiments. This corresponded to a range of δ/a values between 0.7 and 0.07. A particular feature of the study was that the configuration and the amplitude of the mean flow were measured with a directional probe and a hot-film anemometer. It was decided to measure some of the precise properties of the turbulence, such as the intensity of fluctuation, local spectrum, the various scales of turbulence and the dissipation rate ϵ. These last data, which are rarely found in the studies mentioned above, constitute important information for any interpretation or modelling of the phenomenon.

The experimental apparatus and the measurement instrumentation are described in §2. Section 3 deals with the study of mean flow. Turbulence is analysed in §4 and in §5 the results are discussed.

2. Apparatus and method

2.1. *The induction furnace*

The experimental device consists of a stainless-steel cylindrical crucible placed in a 15-turn coil and filled with mercury. The crucible has an internal radius $a = 100$ mm and a thickness $e = 1$ mm. The height of mercury is $H = 140$ mm. The location of the pool is shown in figure 1.

The inductor is supplied with an electric power source (from 0 to 20 kW) which can provide a single-phase sinusoidal current with various frequencies in the range 50–5000 Hz (table 1). The reference maximum value of the magnetic field has been deduced from Nagoaka's formula:

$$B_0 = 2^{\frac{1}{2}} \frac{\mu N I}{H_c} \left(1 + 0.88 \frac{a_c}{H_c}\right), \tag{4}$$

where H_c, a_c, N respectively denote the height, the radius and the number of turns of the coil. The value of B_0 is used to define the Alfvén speed u_A ((2)), the range of which is indicated in table 1.

In order to control the temperature of the pool, the crucible is surrounded by a water-cooled jacket. Because of the strong turbulence of the flow, the temperature variations in the mercury bath are less than 1 %, as shown by previous measurements (Koanda & Fautrelle 1982).

2.2. *Instrumentation*

The velocity-field investigation of a recirculating liquid-metal flow requires two complementary pieces of information: the flow-pattern determination, and the mean- and fluctuating-velocity magnitude. Therefore two measurement devices are used.

The directional probe. The flow direction can be measured locally using a device for tracking the thermal wake behind a heat source. The heat transmitter is a hot wire, whilst the receiver is simply a temperature probe as shown in figure 2. The receiver is fixed with respect to the transmitter in the radial or vertical direction. Such a directional probe detects the sign of the velocity only for purely radial or vertical flows. Owing to the weakness of the temperature differences in the thermal wake, the investigation of the thermal wake is possible only if the hot wire is supplied with a sinusoidal electric-current source (frequency F). A synchronous detection (frequency

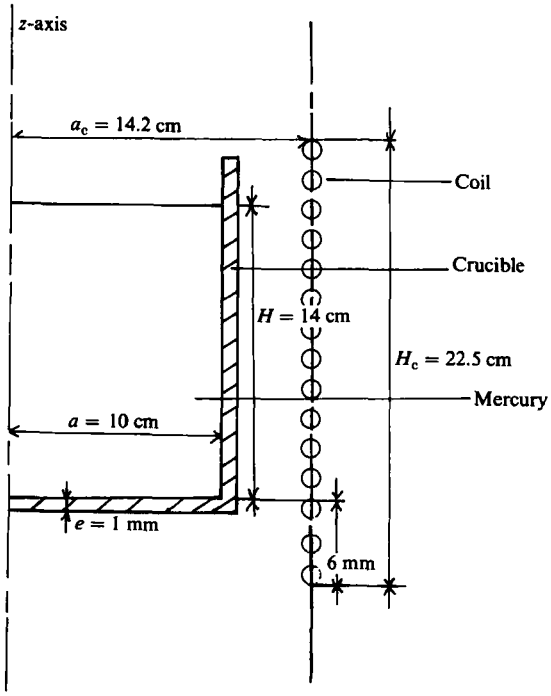

FIGURE 1. Schematic of the apparatus.

Frequency f (Hz)	$R_\omega = 2\pi\mu\sigma f a^2$	Skin depth $\frac{\delta}{a}$	Alfvén speed u_A (cm/s)
50	3.9	0.7	< 28
380	30.0	0.26	< 18.5
2100	166	0.11	< 12.3
4700	372	0.07	< 12.3

TABLE 1

2F) is used to pick out the temperature signal among the background temperature fluctuations in the bath. A sample of such measurements along the axis and the vertical wall of the pool is given in figure 3. The results show unambiguously the separation point between the two vortices.

The anemometry. A cylindrical hot-film miniature probe supplied by a constant-temperature anemometer is used to obtain the average-velocity modulus, turbulent intensity and time spectra. The signal is treated on an AM micro-processor. Particular care has to be taken as far as the cleanliness of the probe is concerned. The calibration function of the probe is (Trakas 1982):

$$\left(\frac{R}{E^2}\right)_{u=0} - \left(\frac{R}{E^2}\right)_u = Au^n, \tag{5}$$

where u is the velocity, E the measured tension, R the resistance of the probe, and A and n are two constants of the calibration function which are independent of the state of cleanliness of the probe.

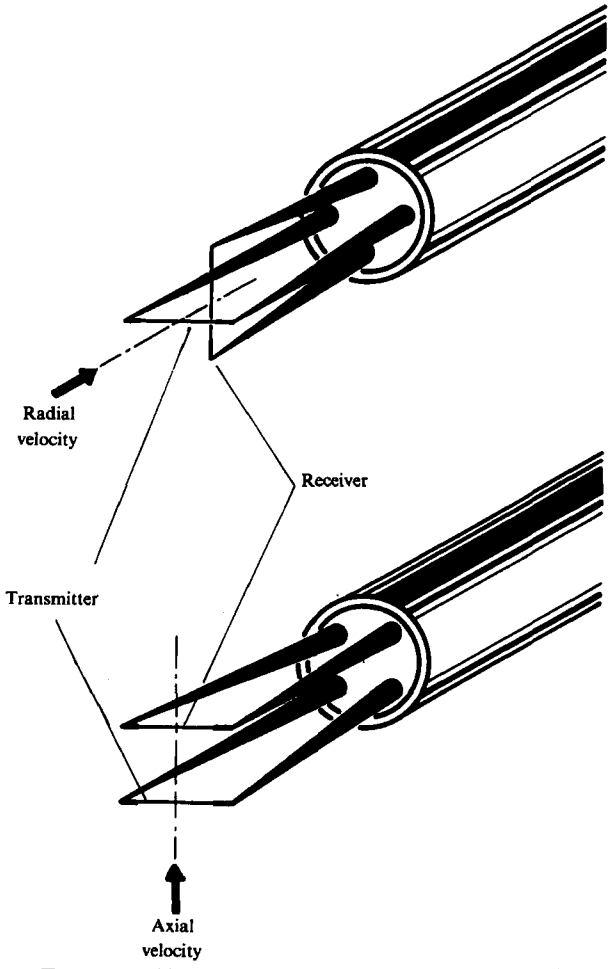

FIGURE 2. Sketch of the two-wire directional probe.

The ratio $(E^2/R)_{u=0}$ represents thermal flux when the speed is equal to zero, i.e. pure-conduction flux. Its value can only be fixed at the beginning of the experiment when the mercury is stationary. In order to make sure that the cleanliness of the probe does not vary, it is necessary to ensure at the end of the experiment that the value $(E^2/R)_{u=0}$ is the same as it was at the start. In order to use this value in (5) it was necessary to check that the average heating of the mercury (about 20 °C) by the Joule effect could not affect this value. A calibration of the pure-conduction flux has shown that, for such variations in temperature, the relative error in the value of $(E^2/R)_{u=0}$ is about 2 %. The corresponding error in the velocity measurements is approximately 20 % (cf. Taberlet 1984).

Special precautions have to be taken to eliminate perturbation of the signal due to the electric currents induced in the measurement device. In all the measurements the ratio between the signal and the noise is about 100.

The superheat of the probe is 7.5 %. We have checked that the superheat was sufficient to minimize the signal pollution due to temperature fluctuations. Nevertheless, in the high-frequency cases, measurements near the walls were less accurate because of stronger temperature fluctuations, which prevented the accurate control of the superheat.

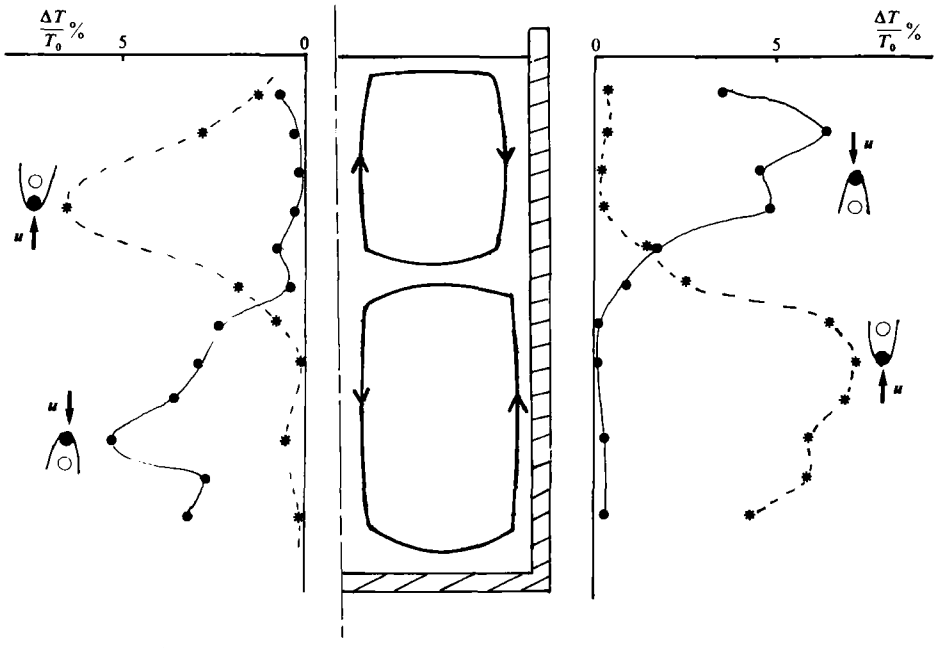

FIGURE 3. Sample measurements of the separation points.

Stabilization of the mean-flow properties required an integration time of about 3 min. Turbulence spectra were obtained by averaging sixty samples, using a standard FFT computation. The spikes observed on the spectra correspond to a frequency of 50 Hz.

3. The mean flow

3.1. *Flow pattern*

Using the directional probe, we were able to map out the mean-flow pattern. The experimental procedure consists of exploring in a meridian plane the regions where the velocity direction may easily be guessed, as shown in figure 3. The uncertainty in the location of the separation point along the axis is about 1 cm. The evolution of the flow configuration has been investigated with respect to the magnetic field (or equivalently the current intensity) and the frequency.

3.1.1. *Influence of the coil current*

The flow pattern was found to be insensitive to coil-current variations, in agreement with previous measurements (Trakas *et al.* 1984; Koanda & Fautrelle 1982).

3.1.2. *Influence of the frequency*

The influence of the frequency was investigated for $f = 50, 380, 2100$, and 4700 Hz. The corresponding skin depths are indicated in table 1. Figure 4 shows the observed flow patterns. It is noticeable that the flow configuration may consist of two or three vortices in a meridian plane according to the frequency. It is difficult to interpret precisely the evolution of the flow configuration. Indeed, the electromagnetic-force distribution depends almost entirely on the frequency of the coil current. This is

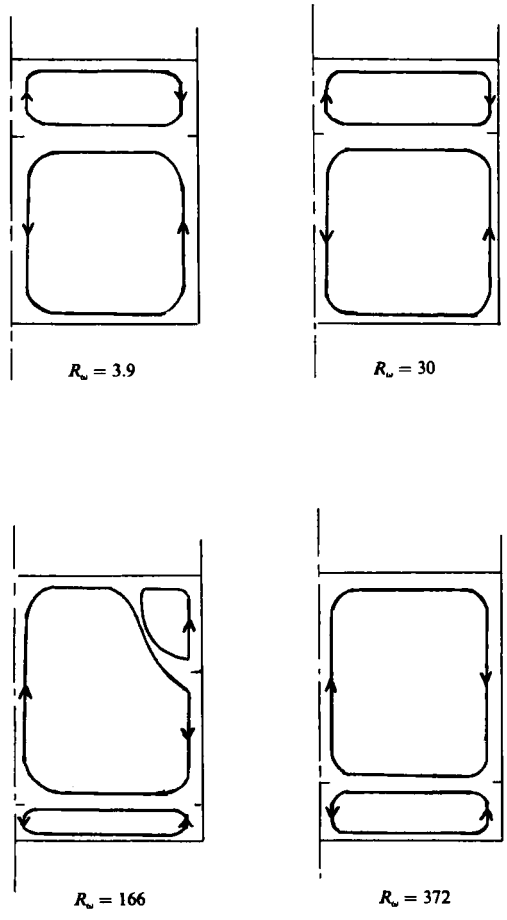

FIGURE 4. Measured flow patterns for various frequencies.

clearly shown by numerical computations performed in the same geometry and illustrated in Appendix A. The flow pattern is nevertheless globally consistent with previous experiments (Moore & Hunt 1983; Trakas *et al.* 1984; Koanda & Fautrelle 1982).

3.2. *Velocity profiles*

The velocity was measured with hot-film probes. Because of the weak polar response of such probes (see for example Robinson & Larsson 1973) it is important to select regions where the measurements are significant. Therefore it was decided to explore radii through vortex cores where the velocity vector is nearly vertical. It was observed that the mean-velocity measurements require long integration time to avoid significant dispersion of the results. This source of inaccuracy is due to the existence of long-period fluctuations (§4 below).

As in the previous section the influences of the coil intensity and the frequency will be considered separately.

3.2.1. *Influence of the intensity*

Figure 5 shows the evolution of the characteristic velocity obtained by averaging the modulus of the velocity along the axis of the pool. In the turbulent regime

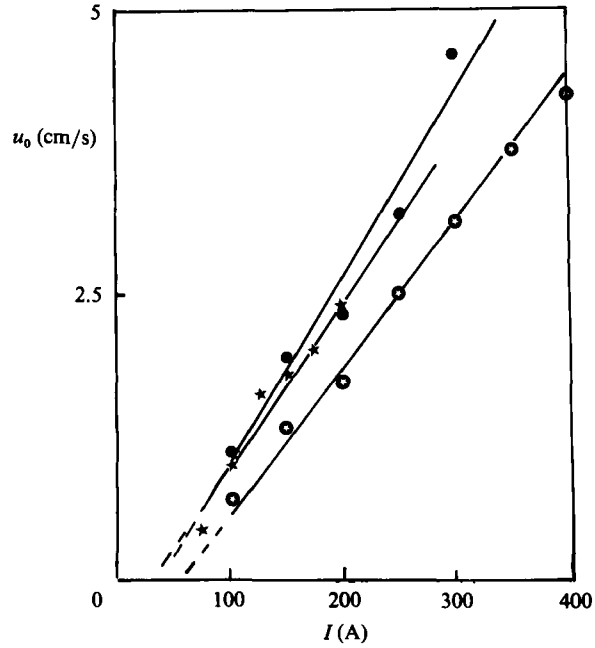

FIGURE 5. Evolution of the characteristic velocity (cf. §3.2.1) with respect to the coil current (r.m.s.) for various frequencies: ✪, $R_\omega = 3.9$; ●, 30; ★, 372.

considered in our experiment the velocity is found to depend linearly on the coil intensity. This result is consistent with previous experiments (e.g. Moore & Hunt 1983; Trakas *et al.* 1984; Koanda & Fautrelle 1982).

3.2.2. *Influence of the frequency*

Owing to the linearity between the velocity and the coil current it is convenient to normalize the velocities by the Alfvén speed u_A. The spatial distributions of the mean vertical-velocity components are shown in figure 6 for various frequencies. The change in the velocity sign has been determined using the directional probe, and it has been checked that the mass-conservation constraint was satisfied. Some dispersion occurs near the inversion point as a consequence of the high local turbulent intensity.

The shape of the velocity profiles is roughly similar for any frequency. The zero-velocity point is approximately at $r/a = 0.7$. In the small-skin-depth limit Batchelor's theorem holds in the central region (e.g. Fautrelle 1981). It is noteworthy that in the infinitely-long-pool case, which represents approximately the region across the vortex core, the theoretical separation point is at $r/a = 2^{-\frac{1}{2}}$ (cf. Appendix B).

For a fixed coil current the evolution of the maximum and the average of the modulus of the velocity along the axis of the pool (respectively u_w and u_0) with respect to the frequency is illustrated in figure 7. The points where the velocity is a maximum are near the wall. In that region the determination of the maximum is difficult, as mentioned in §2. This explains the lack of accuracy of u_w as indicated in figure 7. It must be pointed out that the curve reaches a maximum for $R_\omega \sim 40$. This result is in accordance with previous conjectures (e.g. Tarapore & Evans 1976; Koanda & Fautrelle 1982) and confirms experimentally the existence of a regime where the stirring is most efficient. For large values of R_ω it is difficult to define precisely the asymptotic behaviour of the typical velocity. Nevertheless, it is clear that the behaviour is not inconsistent with the $R_\omega^{-\frac{1}{4}}$ law predicted in various papers, e.g.

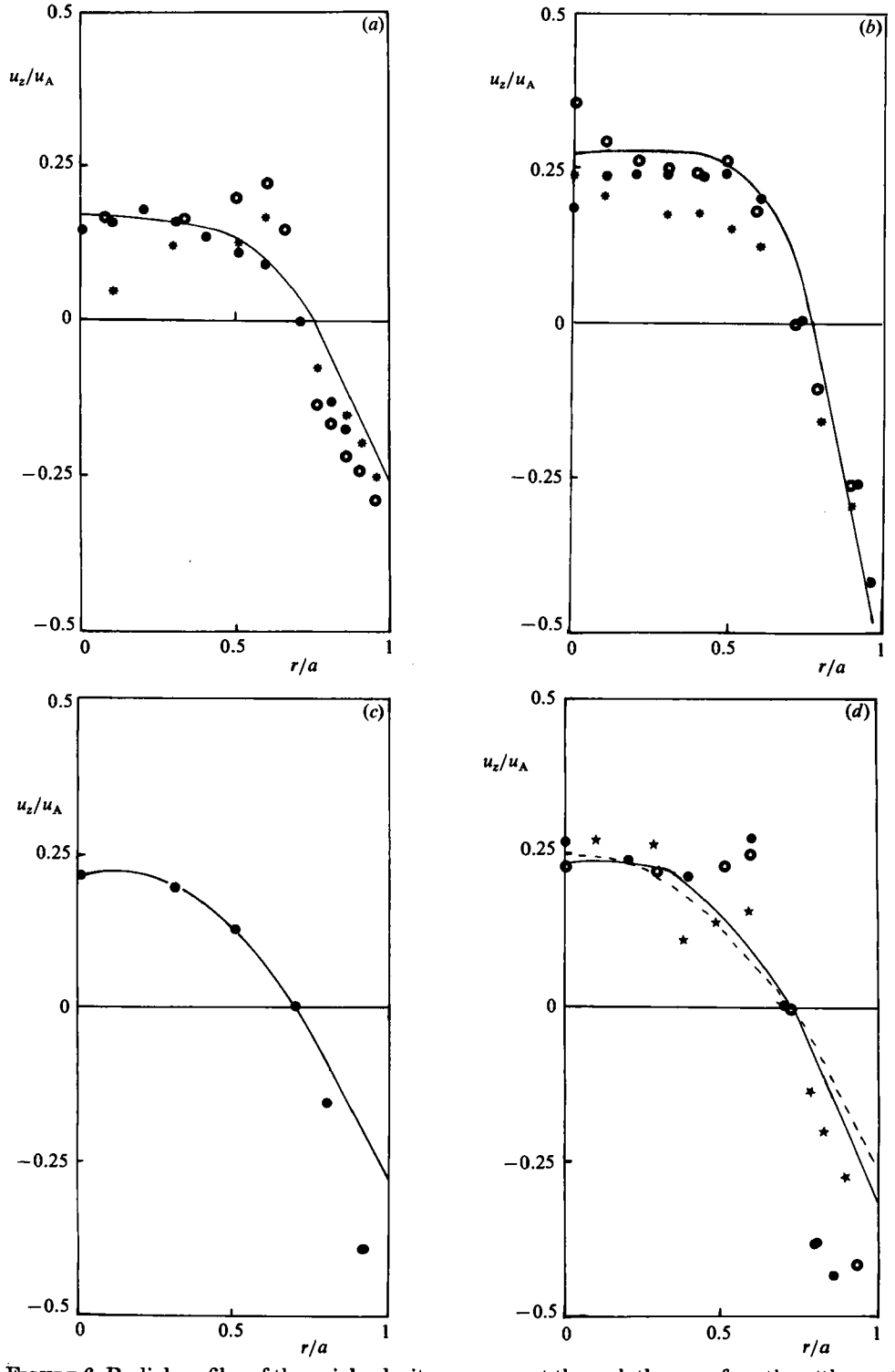

FIGURE 6. Radial profiles of the axial velocity component through the eye of vortices (the vorticity is normalized by the Alfvén speed u_A, and the height z is measured from the bottom of the pool): the profile satisfying mass conservation; --- parabolic profile (see (25)). (*a*) $R_\omega = 3.9$: ✪, $z/H = 0.43$; ●, 0.3; *, 0.78. (*b*) $R_\omega = 30$: ●, $z/H = 0.78$; ✪, 0.5; *, 0.43. (*c*) $R_\omega = 166$: ●, $z/H = 0.7$. (*d*) $R_\omega = 372$: ●, $z/H = 0.08$; ✪, 0.5; ★, 0.15.

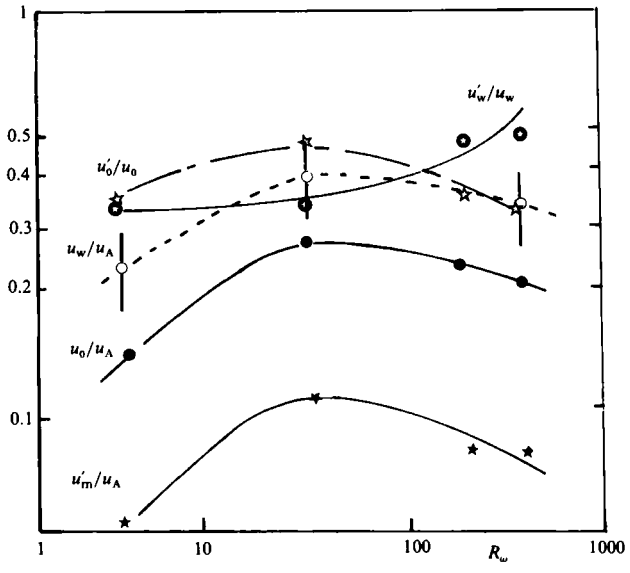

FIGURE 7. Evolution of the mean and turbulent velocities with respect to the frequency (the velocities are normalized by the Alfvén speed u_A): ●, characteristic (cf. §3.2.1) velocity; ○, maximum mean axial velocity component (the bars indicate the absolute error on those values); ★, fluctuating axial velocity component (r.m.s.) averaged along the radius through the core of the vortex; ☆, turbulent intensity on the axis of the pool; ✪, turbulent intensity near the wall.

Lillicrap & Moore (1982), Koanda & Fautrelle (1982). For lower values of R_ω the lack of measurements does not allow confirmation of theoretically calculated behaviour (see Appendix A).

4. Turbulence

4.1. *Turbulent fluctuations*

A simple recording was made of the signal from the anemometer probe over long periods. The signal was shown to contain high frequencies which could be attributed to advected spatially organized turbulence. The signal also contained long time periods (several minutes) which did not seem to correspond to turbulent eddies being advected but rather to some instability of the whole flow pattern. Taylor's hypothesis allows us to distinguish these two factors pertaining to the signal: spatially organized turbulence corresponds to frequencies higher than about 0.1 Hz, i.e. to structures smaller than the size of the crucible.

Spectral analysis of the low frequencies showed that these did not contain characteristic frequencies but had a spectrum close to a white noise whatever the intensity and the frequency of the inductive current. The study of these low frequencies, which contain about $\frac{1}{4}$ of the total energy of the signal, could not be included in a sufficiently developed theoretical frame to lead to the practical utilization of these data. On the other hand, the study of spatially organized turbulence led to knowledge of the flow which is useful for the understanding of transfers in furnaces.

The value of u', the turbulent velocity, calculated from the r.m.s. of the high-frequency signal is obtained after high-pass filtering above 0.1 Hz.

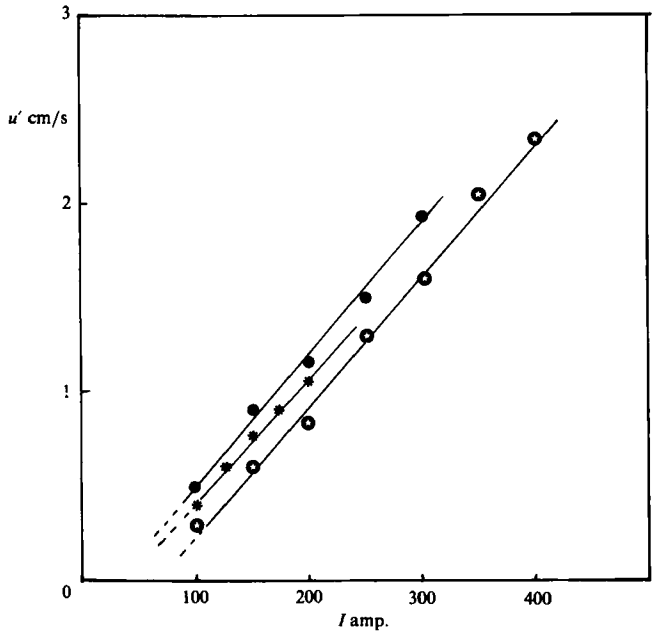

FIGURE 8. Evolution of the fluctuating axial velocity component (r.m.s.) averaged along the axis of the pool with respect to the coil current for various frequencies (the velocity is normalized by the Alfvén speed u_A): ✪, $R_\omega = 3.9$; ●, 30; *, 372.

4.1.1. *Variation of u′ with respect to the intensity*

Figure 8 shows that, whatever the frequency may be, the variation of u' with the intensity of the inductive current is linear. This result had already been obtained by different researchers and confirms theoretical predictions (Trakas *et al.* 1984; Koanda & Fautrelle 1984).

4.1.2. *Profiles of u′*

The profiles of u' (normalized by the Alfvén speed u_A) registered along the radius through the core of vortex for different values of R_ω (figure 9) are reasonably similar. The value of u' exhibits a constant level in almost the whole crucible and a growth near the wall. It should be noted that the growth is more evident where R_ω has high values.

4.1.3. *Variations of u′ with the frequency*

Figure 7 shows the variation of the average value of the turbulent fluctuation u'_m (averaged along the radius of a vortex core) and the turbulent intensities through a vortex core near the wall (u'_w/u_w) and on the axis (u'_0/u_0 as a function of the parameter R_ω. As with the mean flow, the average turbulent fluctuation u'_m reaches a maximum for $R_\omega \simeq 40$. Nevertheless, the respective evolutions of u'_w/u_w and u'_0/u_0 are somewhat different. Near the wall the turbulent intensity u'_w/u_w seems to increase with R_ω, although the intermediate frequency ($R_\omega = 30$) does not confirm that tendency.

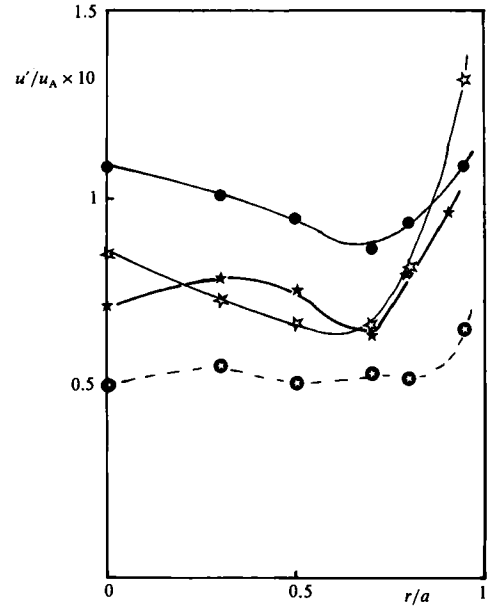

FIGURE 9. Radial profiles of the fluctuating axial velocity component through the eye of the upper vortex for various frequencies (the velocity is normalized by the Alfvén speed u_A): ✪, $R_\omega = 3.9$, $z/H = 0.78$; ●, 30, 0.78; ☆, 166, 0.7; ★, 372, 0.5.

4.2. *Turbulence spectra*

4.2.1. *Description*

Figure 10 presents the one-dimensional spectra $F_{11}(k)$ obtained from a signal measured close to the vertical wall. Here the speed is at its maximum. This signal can be used once the low frequencies have been eliminated (high-pass filtering at 0.1 Hz, cf. §4.1) and after applying Taylor's hypothesis, which allows a spatial description of the turbulence by wavenumber k. The spectra have been compensated (multiplied by $k^{\frac{5}{3}}$) to distinguish the decay zones. The aspect of these spectra is the same for the four envisaged frequencies with a decay zone proportional to $k^{-\frac{5}{3}}$ (corresponding to the plateau) which is interpreted as an inertial region. Furthermore, for large k we observe a faster decrease of the spectra ($\sim k^{-3}$) attributed to a dissipation zone. The injection zone cannot be seen on a one-dimensional spectrum such as this because of the 'aliasing' effect (Tennekes & Lumley 1979). Variations of the current intensity do not noticeably modify the shape of the spectra: only its level is affected. Let it be noted, however, that in the intensity range covered the Reynold's number for the flow varies at most by a factor of 3, which is not sufficient to observe a significant enlargement of the spectrum towards the smaller structures. Therefore it seems that the spectra are self-similar with respect to the intensity, as already mentioned by other researchers (Trakas *et al.* 1984).

4.2.2. *Dissipation*

Generally the rate of dissipation ϵ can be defined by integrating the dissipation spectrum,

$$\epsilon = 15\nu \int_0^\infty k^2 F_{11}(k)\,\mathrm{d}k, \tag{6}$$

if isotropy can be assumed.

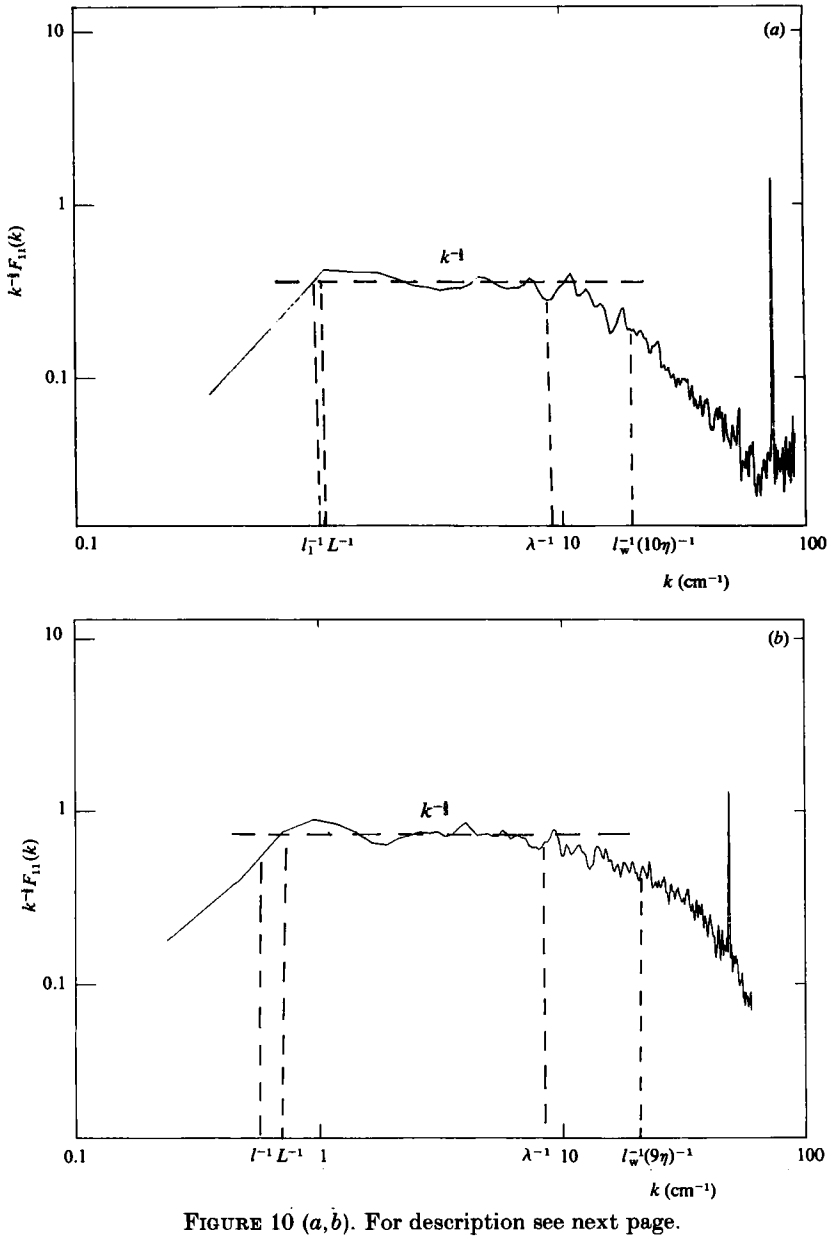

FIGURE 10 (*a*, *b*). For description see next page.

The contribution of high wavenumbers to this integral is very important. It is therefore necessary to measure the dissipation zone accurately. It is, however, difficult to obtain a value which is representative of ϵ because of the limited resolution of the probe (0.5 mm). In order to obtain information about quantity from mono-dimensional spectra, it was necessary to identify the measured inertial zone with those of homogeneous and isotropic turbulence, taking into account the local balance in this region of the spectrum. It is then easy to determine the transfer rate and consequently the dissipation rate ϵ in this zone using Kolmogorov's law:

$$F_{11}(k) = \alpha_1 \epsilon^{\frac{2}{3}} k^{-\frac{5}{3}}. \tag{7}$$

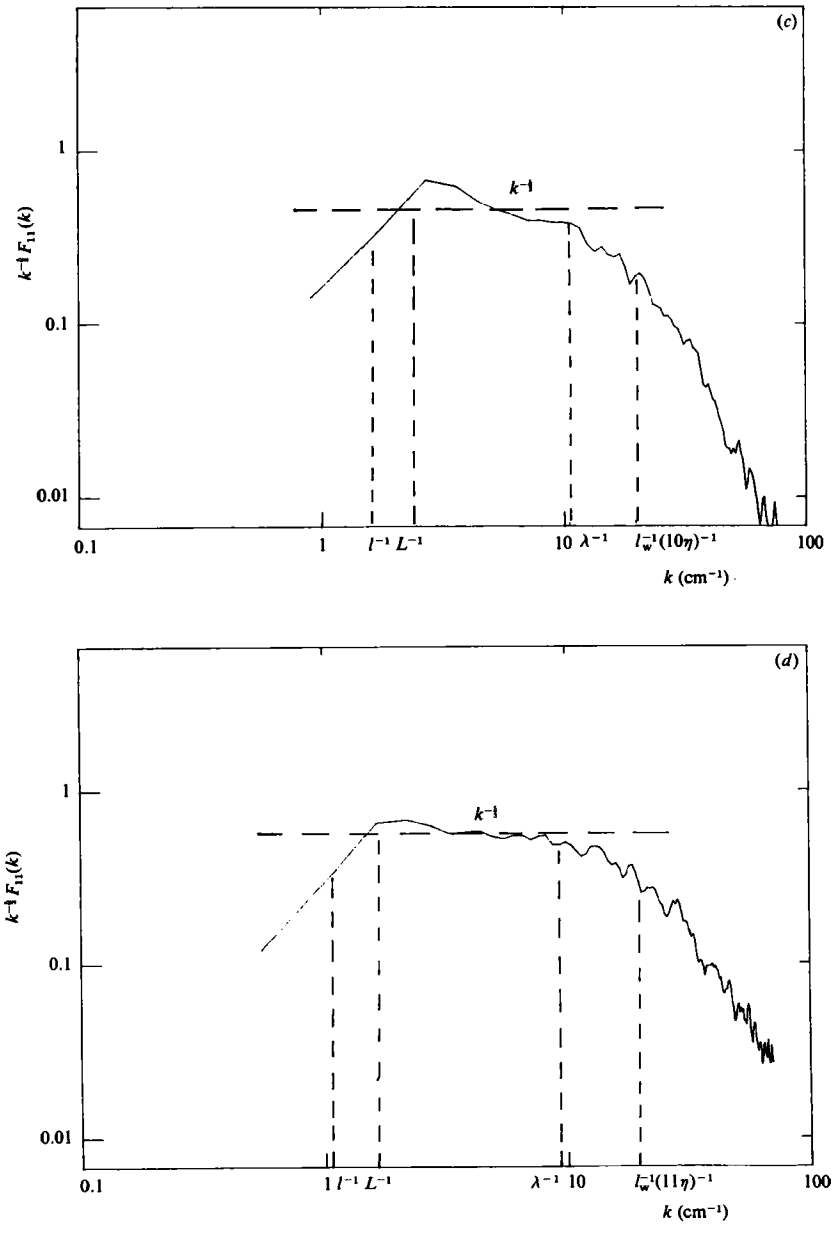

FIGURE 10. One-dimensional wavenumber spectra multiplied by $k^{\frac{1}{3}}$ for various frequencies (L, λ, l_w, η respectively denote the integral scale, the Taylor scale, the probe-sensor length, the Kolmogorov scale; and $l = u'^3/\epsilon$; the units of F_{11} are cm^3 s^{-2}): (*a*) $R_\omega = 3.9$; (*b*) 30; (*c*) 166; (*d*) 372.

The universal constant α_1 is better defined when the Reynolds number R_λ (from Taylor's scale λ) is high. For the spectra obtained with a low R_λ (~ 400), the inertial zone covers about one or two decades, and its value is relatively well defined. The value that was considered was measured inside jets (Champagne 1978) and is

$$\alpha_1 \sim 0.48.$$

The experimental comparison between (6) and (7) shows that the value of ϵ given

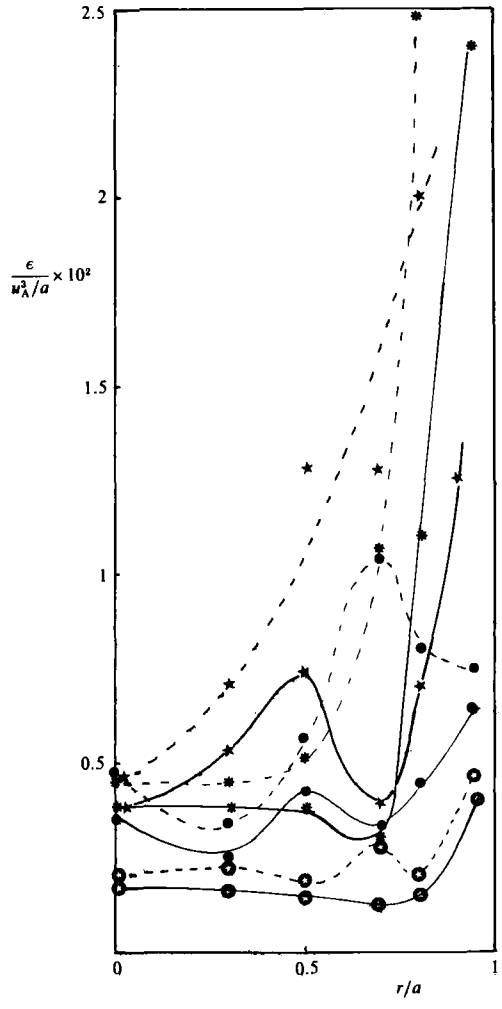

FIGURE 11. Radial profiles of the turbulent dissipation rate through the eye of the upper vortex for various frequencies (——, with Lumley's correction; – – – –, without Lumley's correction; ϵ is normalized by u_A^3/a: ✪, $R_\omega = 3.9$, $z/H = 0.78$; ●, 30, 0.78; ★, 166, 0.7; *, 372, 0.5.

by (6) is much lower than that obtained from (7) (a factor of 4 approximately). We will show that the latter is more realistic.

Figure 11 presents the profiles of ϵ (normalized by u_A^3/a) as registered along the radius through the core of a vortex for different values of R_ω. We have also plotted the values of ϵ obtained after correction using Taylor's hypothesis since the turbulence intensity was high (Lumley 1965). The correction is meaningful, particularly in the neighbourhood of the core of the vortex, where the turbulent intensity reaches 100% or more. The curves all present the same aspect with a significant increase in dissipation when close to the wall, which is accentuated at high frequency.

The average non-dimensional value $\bar{\epsilon}$, which is approximately calculated from these profiles by

$$\bar{\epsilon} = \frac{2}{a^2} \int_0^a r\epsilon(r)\,\mathrm{d}r, \tag{8}$$

allows an estimation of the injected mechanical power P_{em}, which is related to $\bar{\epsilon}$ by:

$$P_{em} = \int_{V_0} \boldsymbol{u} \cdot (\boldsymbol{j} \times \boldsymbol{B}) \, dv = \frac{\rho V_0 u_a^3}{a} \bar{\epsilon}, \tag{9}$$

where V_0 denotes the volume of the bath. P_{em} has also been estimated from numerical computations of electromagnetic forces. The good agreement between the two estimations validates the validity of the prediction of ϵ from (7).

In the conditions in which the experiment was carried out, the mechanical power injected was only several milliwatts.

4.2.3. *Scales of turbulence*

Calculation of the different scales. Once ϵ is known three types of scales can be estimated:

– the large-structures scale

$$l = \frac{u'^3}{\epsilon}; \tag{10}$$

– Taylor's transversal scale λ such that

$$\epsilon = 15\nu \frac{u'^2}{\lambda^2}; \tag{11}$$

– the small-structures scale also called Kolmogorov's scale

$$\eta = \left(\frac{\nu^3}{\epsilon}\right)^{\frac{1}{4}}.$$

These scales shown on the spectra allow the checking of the consistency of the results with those of homogeneous and isotropic turbulence.

These scales as well as the scale l_w corresponding to the probe dimension (0.5 mm) are shown on the compensated spectra (figure 10). In any event, the scale for large structures l is at the beginning of the inertial zone and Taylor's scale, which is between the large and small structures, is in the inertial zone close to the dissipation zone. Taking into account the small value of R_λ (~ 200), this zone starts at about $k = 0.1\eta^{-1}$. These results are very much in agreement with various experimental results found by researchers who have worked in the same ranges of R_λ and referenced by Hinze (1975).

The location of scale l_w of the probe sensor allows the definition of confidence fields on the spectra. The values show $l_w \sim 10\eta$, which confirms that the dissipation zone was not described in a precise fashion.

Integral scale. The value for $k = 0$ on the one-dimensional spectra allows a definition of the scale of energetic structures, also called the integral scale, namely

$$L = \frac{\pi F_{11}(0)}{u'^2}.$$

This scale is also shown on the spectra of figure 10. Note that L is similar to l. It may be shown from (9) that $\epsilon \sim I^3$. Since u' is found to be proportional to I, (10) implies that l or L is independent of I, which is confirmed experimentally. It can equally be found using the Prandtl theory, according to which the turn-over time of the energy-containing eddies l/u' is of the same order of magnitude as the characteristic timescale of the mean flow:

$$l/u' = \Lambda/u, \tag{12}$$

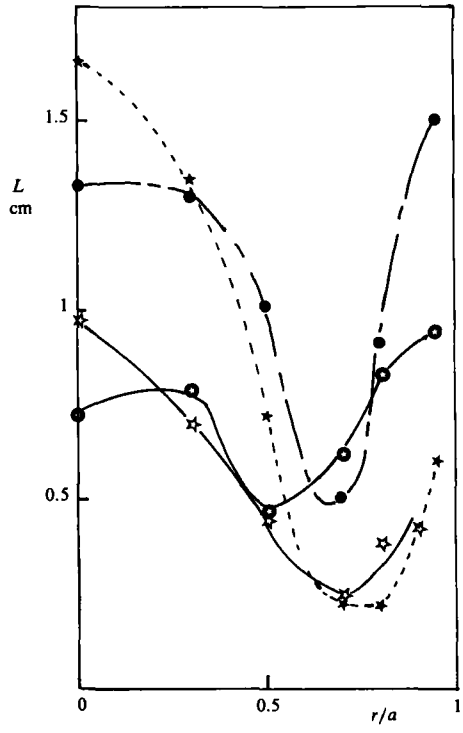

FIGURE 12. Radial profiles of the integral scale through the eye of the upper vortex for various frequencies: ✪, $R_\omega = 3.9$, $z/H = 0.78$; ●, 30, 0.78; ☆, 166, 0.7; ★, 372, 0.5.

A denoting the typical variation scale of the mean flow. A involves the mean-flow gradients which are not sensitive to inductor-current variations. Figure 12 shows the profiles of L as registered along the radius through the core of the vortex. Such a minimum may not be significant because of the high local turbulent intensity. Nevertheless it must be observed that, for large values of R_ω, L is globally decaying from the axis of the pool to the wall. In any case, the order of magnitude of the integral scale is 1 cm.

5. Discussion

The main results of this paper concern the exploration of the mean and turbulent flow field with respect to the two main parameters which control the phenomenon, namely the intensity and the frequency of the inductive current.

The magnitude of the coil current controls the amplitude of mean and turbulent velocities, which are proportional to it. On the other hand, it has no influence whatsoever either on the configuration of the flow or more evidently even on the large scales of the turbulence (i.e. the integral scale). Consequently, the mean and turbulent motion appears on a large scale as being self-similar. This had already been discovered by Trakas *et al.* (1984).

The frequency has been shown to influence the amplitude of mean velocities. It passes through a maximum when the electromagnetic skin is approximately equal to $0.2a$. The configurations observed depend on frequency only via the different distribution of electromagnetic forces. In fact the confinement of the forces at a high frequency does not significantly modify the shape of the velocity distribution through

R_ω	$\frac{l}{u'}\Big/\frac{a}{u_A}$ on the axis	$\frac{l}{u'}\Big/\frac{a}{u_A}$ near the wall	$\frac{\Lambda}{a}$ on the axis	$\frac{\Lambda}{a}$ near the wall
3.9	1.5	1.4	0.2	0.3
30	1.2	1.4	0.3	0.5
166	1.4	0.4	0.3	0.06
372	1.8	0.4	0.5	0.10

TABLE 2. Evolution of the turnover time l/u' and the corresponding typical variation scale of the mean motion Λ versus R_ω through the eye of the vortex on the axis ($r/a = 0$) and near the wall ($r/a = 0.95$) from (12)

a vortex as shown in the profiles of mean velocity through the vortex core. In the case of high frequencies, it is important to notice that the scale δ does not strongly influence the turbulence. This last result is illustrated by the shape of the spectra of turbulence, which remain quite similar for any frequency. We note, however, a non-negligible global decrease of L as R_ω increases, especially near the wall. The influence of the frequency also appears in the evolution of the spatial distribution of the rate of turbulent dissipation. In fact the rate of turbulent dissipation is characterized by a noticeable increase in the neighbourhood of the wall. This is linked to the local increase of the turbulent fluctuations there. The increase of the turbulent intensity in the electromagnetic skin may be explained by simple arguments similar to Prandtl theory. The order of magnitude of u' can be related to the gradients of the mean flow as suggested by (12). The value of Λ is of order a for low R_ω or decreases near the wall for large R_ω as shown by the experimental values of table 2. Although l decreases with respect to R_ω, the turbulent intensity globally remains a growing function of R_ω. The growth of u' in the neighbourhood of the wall for large R_ω is also consistent with Batchelor's theorem (1956). As (17) of Appendix B shows, the existence of a steady mean motion requires equilibrium between the electromagnetic driving force and sufficiently large Reynolds stresses for each mean streamline which crosses the electromagnetic skin. It should be noted that when the forces are totally spread within the bath (e.g. $R_\omega = 3.9$) u' or ϵ is spread in the whole of the volume. These results suggest the following evolution according to the frequency:

(i) The low-frequency limit ($\delta/a \sim 1$): the Reynolds stresses balance the Lorentz forces in the whole bath; Λ is of order of a, or equivalently the turnover time l/u' of the energy-containing eddies is of the order of the characteristic timescale of the mean motion everywhere in the pool, as shown in table 2;

(ii) The high-frequency limit ($\delta/a \ll 1$): the balance between the Reynolds stresses and the Lorentz forces is required only in the electromagnetic skin; the vorticity is created in the electromagnetic layer and diffused (by the turbulence) in the bulk of the domain according to Batchelor's theorem; Λ is of order a in the central region and decreases in the electromagnetic layer, consistent with the evolution of L from the axis to the wall (figure 12).

The orders of magnitude of the mean velocity obtained from the above conjectures (cf. (21), (23), Appendix B) are in accordance with the experimental results. It should be noted that in the frequency range considered the Alfvén speed remains a good estimate of the mean velocities.

The existence of long-period fluctuations has already been discussed by Moore & Hunt (1983, 1984) and Trakas *et al.* (1984). It is interesting to note that these periods were much shorter (~ 10 s) than those observed in the present work (several

minutes). Moreover, contrary to Trakas *et al.* (1984) the analysis of the spectra at low fluctuation frequency does not show privileged frequencies (see §4). The existence of such long periods which have been observed in recirculating flows, is consistent with an instability mechanism such as the Coanda effect proposed by Moore & Hunt (1983).

From a metallurgical point of view, the electromagnetic stirring is an efficient means of achieving a good homogeneity of the bath. Such a flow is indeed characterized by a high turbulent intensity (about 40%). It should be noted that stirring decreases more rapidly at low frequency (i.e. low values for R_ω) than at high frequencies or for large values of R_ω. This may have a practical application in the choice of the optimum frequency of the power supply.

It is interesting to note that the decrease in the electromagnetic-skin depth modifies significantly the properties of the turbulence in the vicinity of the walls and consequently the transfer at the boundaries of the pool. This phenomenon can have important metallurgical consequences on chemical-reaction kinetics such as metal–slag transfers through the free surface of the bath.

In our experiments, we could not observe the influence of the pulsating part of the Lorentz forces because of the large inertia of the mercury. It would be of interest to use lower coil-current frequencies to study the effects of an alternating body force on the turbulence of the flow, especially when the excitation frequency is of the order of the characteristic frequency of the large eddies. This phenomenon could have interesting metallurgical applications.

Appendix A. The Lorentz-force distribution

In order to understand the observed flow configurations, it is pertinent to recall the evolution of the Lorentz-force distribution for various frequencies and for a given coil current. To this end the force field has been determined using a well-known numerical computation procedure consisting of computing the single component of the vector potential by means of a finite-difference method (see for example Barbier *et al.* 1982). The computed distributions of the Lorentz forces are shown in figure 13 for various values of R_ω. Because of the corner effects, it is clear that variations of the frequency lead to important changes in the electromagnetic-force distribution.

The maximum value of the Lorentz forces is located either in the middle depth of the pool when $R_\omega \sim 1$ or in the corner regions for large R_ω.

Let us investigate the behaviour of the force field in the low-frequency limit. Using B_0 and a respectively as magnetic field and lengthscales yields the non-dimensional Maxwell equations

$$\left.\begin{aligned} \nabla \times \boldsymbol{A} &= \boldsymbol{B}, \\ \boldsymbol{j} = \boldsymbol{E} &= -\frac{\partial \boldsymbol{A}}{\partial t}, \\ \nabla \times \boldsymbol{B} &= R_\omega \boldsymbol{j}, \end{aligned}\right\} \tag{13}$$

where $\boldsymbol{A}$, $\boldsymbol{B}$, $\boldsymbol{j}$, $\boldsymbol{E}$ respectively denote the vector potential, the magnetic field, the current density and the electric field. In (13) the electric currents induced by the motion have been neglected with respect to those induced by the pulsation of the magnetic field. This assumption remains valid only if $R_\mathrm{m} \ll R_\omega$, R_m being the magnetic Reynolds number defined from the characteristic velocity as follows:

$$R_\mathrm{m} = \mu\sigma u a.$$

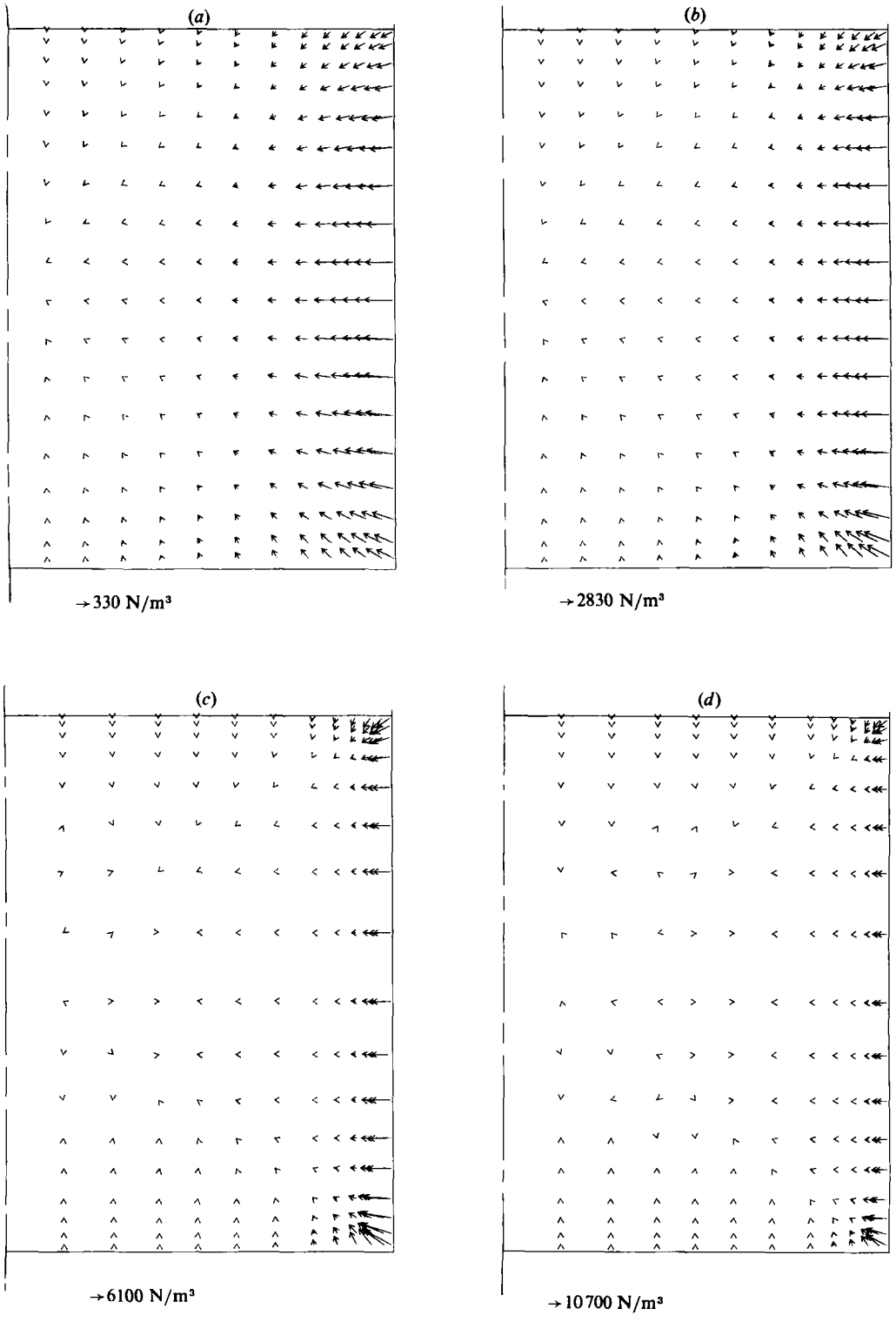

FIGURE 13. Numerical computation of the electromagnetic forces: (*a*) $R_\omega = 3.9$; (*b*) 30; (*c*) 166; (*d*) 372.

In the limit $R_\omega \ll 1$, the variables may be expanded in power series of R_ω:

$$\begin{aligned} \boldsymbol{B} &= \boldsymbol{B}^{(0)} + R_\omega \boldsymbol{B}^{(1)} + \ldots; \\ \boldsymbol{j} &= \boldsymbol{j}^{(0)} + R_\omega \boldsymbol{j}^{(1)} + \ldots; \\ \boldsymbol{A} &= \boldsymbol{A}^{(0)} + R_\omega \boldsymbol{A}^{(1)} + \ldots. \end{aligned}$$

At the lowest order, system (13) reduces to

$$\left.\begin{aligned} \nabla \times \boldsymbol{B}^{(0)} &= 0, \\ \nabla \times \boldsymbol{A}^{(0)} &= \boldsymbol{B}^{(0)}, \\ \boldsymbol{j}^{(0)} &= -\frac{\partial \boldsymbol{A}^{(0)}}{\partial t}. \end{aligned}\right\} \tag{14}$$

It is clear from (14) that the phase of the magnetic field is constant in the whole space and the phase shift between $\boldsymbol{B}^{(0)}$ and $\boldsymbol{j}^{(0)}$ is simply $\frac{1}{2}\pi$.

The dimensional expression $\boldsymbol{F}$ of the electromagnetic forces is

$$\boldsymbol{F} = R_\omega \frac{B_0^2}{\mu a} \boldsymbol{j} \times \boldsymbol{B}. \tag{15}$$

At the lowest order, the time-averaged mean part of the Lorentz forces is from (15) identically zero. Thus the order of magnitude of the mean electromagnetic forces are at the lowest $O(R_\omega^2)$. The latter estimate will be used in Appendix B.

Appendix B. Analysis of the mean-velocity field

It is of interest to interpret the results concerning the observed mean-velocity field using simple theoretical considerations. Using an eddy-viscosity-type turbulent model let us consider the equations of motion governing the steady mean-velocity field $\boldsymbol{u}$:

$$\left.\begin{aligned} \omega \times \boldsymbol{u} &= -\frac{1}{\rho} \nabla p + \frac{\boldsymbol{F}}{\rho} + \nabla \cdot (2\nu_t \boldsymbol{e}), \\ \nabla \cdot \boldsymbol{u} &= 0, \end{aligned}\right\} \tag{16}$$

where p, ω, $\boldsymbol{e}$, ν_t respectively denote the pressure, the vorticity, the deformation rate tensor and the effective viscosity $u'l$. The integration of (16) along a closed streamline C surrounding the surface Σ leads to a modified form of Batchelor's theorem (Batchelor 1956; Sneyd 1971):

$$\frac{1}{\rho} \int_\Sigma \nabla \times \boldsymbol{F} \cdot \mathrm{d}\boldsymbol{s} + \oint_C \nabla \cdot (2\nu_t \boldsymbol{e}) \cdot \mathrm{d}\boldsymbol{l} + 0. \tag{17}$$

Let us determine the orders of magnitude u of the mean flow. Let Λ be an estimate of the scale of variation of the mean velocity field. Using Prandtl theory, we may deduce the order of magnitude of the turbulent fluctuation u' from the mean-velocity gradients as follows:

$$u' = lu/\Lambda, \tag{18}$$

l being defined in (10).

Furthermore, let us write the order of magnitude of $\nabla \times \boldsymbol{F}$ as

$$\nabla \times \boldsymbol{F} = O(c\rho u_A^2/a^2), \tag{19}$$

where c is a numerical coefficient which depends on R_ω.

Equation (17) yields an estimate of u,

$$\frac{u}{u_A} = \left(\frac{c\Lambda^3\Sigma}{\mathscr{L}a^2l^2}\right)^{\frac{1}{2}}, \tag{20}$$

where Σ, $\mathscr{L}$ respectively denote the area enclosed by the streamline C and its length.

One may consider for simplicity two asymptotic cases according to the value of δ/a.

The large-skin-depth limit

In the large-skin-depth limit, the electromagnetic forces are distributed in the whole bath. Equation (17) must hold for all the mean streamlines. This constraint requires that effective viscous diffusion is present in the whole bath in order to balance the electromagnetic forces. Therefore, it is natural to assume that Λ is of order of a. The corresponding velocity estimate is:

$$u/u_A = c^{\frac{1}{2}}a/l. \tag{21}$$

From (15), we may expect the typical velocity u to vary as R_ω in the weak-frequency limit. As an illustration, let us consider the case $R_\omega = 3.9$. The computed maximum value of c is 2.0×10^{-2}. Taking $l/a = 0.1$ from the measurements yields the numerical value of the ratio u/u_A:

$$u/u_A = 1.4. \tag{22}$$

The latter value overestimates the characteristic mean velocities as compared with the experimental ones. This is a consequence of the estimate of Λ which is actually smaller than a, as shown in table 2.

The small-skin-depth limit

In the small-skin-depth limit, the domain may be split into two regions: (i) the electromagnetic layer; (ii) a central region where the effective Reynolds number remains large.

Viscous diffusion is only relevant for the streamlines which cross the electromagnetic layer. Assuming $\Lambda \sim l$ yields the mean-velocity estimate

$$u/u_A = c^{\frac{1}{2}}\left(\frac{l\delta}{a^2}\right)^{\frac{1}{2}}. \tag{23}$$

Note that (23) is somewhat different from that obtained by Moore & Hunt (1983).

In the case $R_\omega = 372$ the value of c is 12.6. With $l \sim 0.01$ m the ratio u/u_A is 0.25. It may be noted that in the limit $\delta/a \ll 1$ the order of magnitude of c is a/δ. If we assume $l \sim \delta$ in (23), the latter estimate is in agreement with the previous $R_\omega^{-\frac{1}{4}}$ law predicted by various authors (Lillicrap & Moore 1982).

As for the flow patterns, the inviscid interior region is characterized by a diffusion of the vorticity. This turbulent-diffusion effect is necessary to reach the steady state. If the gradients of ν_t are weak, then according to the original form of Batchelor's theorem the vorticity must be such that

$$\omega/r = \text{a constant for each vortex}, \tag{24}$$

where (r, θ, z) denote the cylindrical coordinates.

It is interesting to consider the case of a steady vertical unidirectional flow. This

case approximately represents the flow in the vicinity of a radius through a vortex core. The velocity field is in the following form:

$$\boldsymbol{u} = (0, 0, u_z(r))$$

in cylindrical coordinates. The function $u_z(r)$ is readily obtained from (24) and mass conservation up to a constant u_0, namely

$$u_z(r) = u_0\left(\frac{2r^2}{a^2} - 1\right). \tag{25}$$

The latter velocity distribution, which is shown in figure 6(*d*), is parabolic, and $u_z(r)$ is zero for $r/a = 2^{-\frac{1}{2}}$.

REFERENCES

Barbier, J. N., Fautrelle, Y. R., Evans, J. W. & Cremer, P. 1982 *J. Méc. Théor. Appl.* **1**, 533–556.

Batchelor, G. K. 1956 *J. Fluid Mech.* **1**, 177.

Bednarz, T. K. 1970 Ph.D. thesis, Carnegie Mellon University, Pittsburgh U.S.A.

Champagne, F. H. 1978 *J. Fluid Mech.* **86**, 67–108.

Cremer, P. & Alemany, A. 1981 *J. Méc. Appl.* **5**, 37–50.

Fautrelle, Y. 1981 *J. Fluid Mech.* **102**, 405–430.

Hinze, J. O. 1975 *Turbulence* 2nd edn. MacGraw-Hill.

Koanda, S. & Fautrelle, Y. R. 1984 Modelling of coreless induction furnace: some theoretical and experimental results. In *Proc. IUTAM Symp. on Metallurgical Applications of MHD (1982) Cambridge (UK)*. Institute of Metals, London.

Lillicrap, D. C. & Moore, D. J. 1982 In *Proc. Electroheat for metal conference, Cambridge, U.K.*

Lumley, J. L. 1965 *Phys. Fluids* **8**, 1056–1062.

Moore, D. J. & Hunt, J. C. R. 1983 Liquid metal flows and magnetohydrodynamics. Ed. N. Branover, and A. Yakhot. *Prog. Astronautics & Aeronautics* **84**, 359.

Moore, D. J. & Hunt, J. C. R. 1984 Turbulence and unsteadiness in the coreless induction furnace. In *Proc IUTAM Symp. on Metallurgical Applications of MHD (1982) Cambridge (UK)*. Inst. of Metals, London.

Robinson, T. & Larsson, K. 1973 *J. Fluid Mech.* **60**, 641–664.

Sneyd, A. 1971 *J. Fluid Mech.* **49**, 817.

Taberlet, E. 1984 Thèse de Docteur Ingénieur INPG, Grenoble.

Tarapore, E. D. & Evans, J. W. 1976 *Met. Trans.* B **7B**, 345–351.

Tennekes, H. & Lumley, J. L. 1972 *A First Course in Turbulence*. The MIT Press.

Trakas, C. 1982 Thèse de Docteur Ingénieur, CNAM.

Trakas, C., Tabeling, P. & Chabrerie, J. P. 1984 *J. Méc. Théor. Appl.* **3**, 345–370.